UNIVERSITY OF
BATH

University of Bath

Alternative formats

If you require this document in an alternative format, please contact:
openaccess@bath.ac.uk

Mapping the flux penetration profile in a 2G-HTS tape at the microscopic scale: deviations from a classical critical state model

Estefani Marchiori[1] **and Simon J Bending**[1]

[1] Department of Physics, University of Bath, Claverton Down, Bath BA2 7AY, UK

E-mail: `emp33@bath.ac.uk, s.bending@bath.ac.uk`

Abstract. Understanding vortex behaviour at microscopic scales is of extreme importance for the development of higher performance coated conductors with larger critical currents. Here, we study and map the critical state in a YBCO-based coated conductor at different temperatures using two distinct operation modes of scanning Hall microscopy. An analytical Bean critical state model for long superconducting strips is compared with our measurements and used to estimate the critical current density. We find several striking deviations from the model; pronounced flux front roughening is observed as the temperature is reduced below $83\,\text{K}$ due to vortex-bundle formation when strong broadening of the flux front profile is also seen. In higher magnetic fields at the lower temperature of $65\,\text{K}$, fishtail-like magnetization peaks observed in local magnetization measurements are attributed to flux-locking due to an increase in the critical current density near the edges of the tape, which we tentatively link to vortex pinning matching effects. Our measurements provide valuable insights into the rich vortex phenomena present in coated conductor tapes at the microscopic scale.

Keywords: coated conductors, second generation superconducting tape, scanning Hall microscopy, flux front

1. Introduction

Since the discovery of high temperature cuprate superconductors they have been the subject of intensive research due to their fundamental and technological importance. $\text{YBa}_2\text{Cu}_3\text{O}_{7-\delta}$-based coated conductors possess particularly strong potential for use in diverse commercial applications, for example, electrical power transmission lines [1], fault current limiters [2], and rotating machines such as motors and generators [3]. Despite great progress in this field, preventing the rapid suppression of the superconducting critical current density in moderate magnetic fields remains a

major challenge. Once in the mixed state flux line motion driven by an applied current causes dissipation to take place. Preservation of the dissipation-free state requires the presence of effective pinning sites that tailor the energy landscape for superconducting vortices in a controlled fashion.

Several types of pinning sites have been investigated in $YBa_2Cu_3O_{7-\delta}$ (YBCO) thin films, including chemical modification by ion irradiation [4], rare earth nanoprecipitates [5], and irregular artificial arrays [6], which have been shown to strongly enhance the critical current. Nevertheless, the vortex pinning mechanism has not yet been completely controlled and understood. An improved understanding of the pinning potential landscape and flux line behaviour will enable the development of higher performance coated conductors exhibiting higher critical current densities, which can potentially reduce the amount of superconducting material required and consequently lower the production costs, allowing more widespread implementation [7]. Current second-generation high temperature superconducting (2G-HTS) tapes are commonly doped with rare-earth ions to give rise to second phase nanoparticles during the metalorganic deposition (MOD) process. In addition, grain boundaries, vacancies (pores), stacking faults, twin boundaries and point defects also play a role in enhancing the vortex pinning. 2G-HTS tapes are frequently characterised by transport and magnetization measurements, which primarily elucidate the global macroscopic properties of flux lines and pinning sites. Scanning Hall microscopy (SHM) has previously been used to study the supercurrent flow through artificial grain boundaries [8] and to probe ac losses [9] in YBCO films over large scan areas. Here scanning Hall microscopy is used to probe the local properties of the flux front penetration down to a lengthscale of $\sim 1\,\mu$m, allowing us to resolve inhomogeneous current flow and deviations from classical critical state flux distributions at this microscopic scale.

2. Methods

The sample studied was a section of 12 mm wide commercial second-generation high temperature superconducting Amperium tape from American Superconductor, AMSC. Manufactured using Rolling Assisted Biaxially Textured Substrate (RABiTS) technology this tape is doped with Dy_2O_3 nanoparticles to enhance vortex pinning. To achieve direct access to the $YBa_2Cu_3O_{7-\delta}$ film, the copper stabilizer layers have first been removed by wet chemical etching in ferric chloride. The remaining layer of solder on top of the approximately $1.3\,\mu$m thick YBCO thin film has been carefully thinned by polishing with fine alumina paste until the superconducting layer just started to be exposed in a few isolated places. Scanning Hall microscopy (SHM) has been used to directly image the magnetic field component perpendicular to the surface of a 10 x 14 mm^2 piece of 2G-HTS tape prepared in this way at different temperatures. This sample was 2 mm narrower than the original tape due to the removal of the solder fillets at the edges. The microscope used is a modified commercial low temperature scanning tunnelling microscope (STM) where the tunnelling tip has been replaced by a custom-fabricated GaAs chip. The Hall probe is patterned in the two-dimensional electron gas of a GaAs/AlGaAs heterostructure, defined by the intersection of two $0.8\,\mu$m wide wires situated $\sim 5\,\mu$m from the Au coated corner of a deep mesa etch that acts as an integrated STM tip. The Hall probe is mounted at an angle of 1°-2° with respect to the sample plane, with the STM tip being the closest point to the sample surface [10]. The Hall probe with $\sim 0.8\,\mu$m spatial resolution and $\sim 5\,$mG$/\sqrt{Hz}$

minimum detectable field was approached at a point approximately 1 mm from one of the long edges of the tape and then retracted ∼1 μm for fast data collection. Two operation modes were used; a rapid "flying mode" where the Hall sensor makes a rapid 2D scan of the maximum field of view, and a 'local' magnetometry mode whereby the sensor is parked above a desired location and the 'local' magnetic induction measured while sweeping an external magnetic field perpendicular to the plane of the sample. By systematically acquiring SHM images at regularly spaced points on a magnetic field cycle starting from the zero field cooled state, a spatial map can be made of the critical state established around a hysteresis loop.

3. Results and Discussion

Before sample preparation the 2G-HTS tape was found to have a mid-point resistive superconducting critical temperature of $T_c = 92.0 \pm 0.2$ K. However after being etched and polished to expose the YBCO film it exhibited a slightly lower value of $T_c = 89.5 \pm 0.2$ K as shown in Figure 1(a). Local magnetization curves measured at different fixed temperatures are shown in Figure 1(b). The solid red lines are fits of the data at each temperature to a critical state model due to Brandt and Indenbom [11]. Each loop has been scaled by the estimated value of H_c which is directly proportional to the critical current density (j_c) at each temperature. The critical current densities obtained from the model fitting at different temperatures have been plotted in Figure 1(c), and show good agreement with other reported temperature-dependent critical currents for this tape [12].

The data collected on the critical state in the sample of commercial 2G-HTS tape, have been analysed using a critical state model developed by Brandt and Indenbom for an infinite superconducting strip [11]. This describes the magnetic field penetration profile, B_z, in a thin type II superconducting strip of width $2a$ and thickness d in a constant perpendicular magnetic field, H_a, in the limit $d \ll a$. While this continuum model makes many assumptions, for example a homogeneous distribution of pinning sites with a B_z independent critical current, it has the distinct advantage that it is analytic and contains only one fit parameter, j_c, the critical current density.

$$
B_z(y) = \begin{cases}
0 & |y| < b \\
B_c \tan^{-1} \dfrac{\sqrt{y^2 + b^2}}{c|y|} & b < |y| < a \\
B_c \tan^{-1} \dfrac{c|y|}{\sqrt{y^2 + b^2}} & |y| > a
\end{cases}
\tag{1}
$$

Here, $B_c = \mu_0 j_c d/\pi$, $b = a/\cosh(\mu_0 H_a/B_c)$ defines the boundary of the central flux free region, and $c = \tanh(\mu_0 H_a/B_c)$. A schematic diagram of the 2G-HTS tape sample is shown in Figure 2(a), where d is the YBCO film thickness and the blue square depicts the location of the SHM scan area (not drawn to scale). Note that the superconducting strip only has an aspect ratio of 1.4 and is not infinite as assumed in the model. Nevertheless, equation 1 is expected to describe the flux penetration profile rather well near the middle of the long sides. The magnetic field profile predicted by equation 1 across the 10 mm wide tape is shown in Figure 2(b) for different applied field intensities increasing from zero field.

Since the applied field reverses sweep direction during magnetometry measurements once it reaches the maximum fields, $\pm H_{max}$, we also make use of the relationship
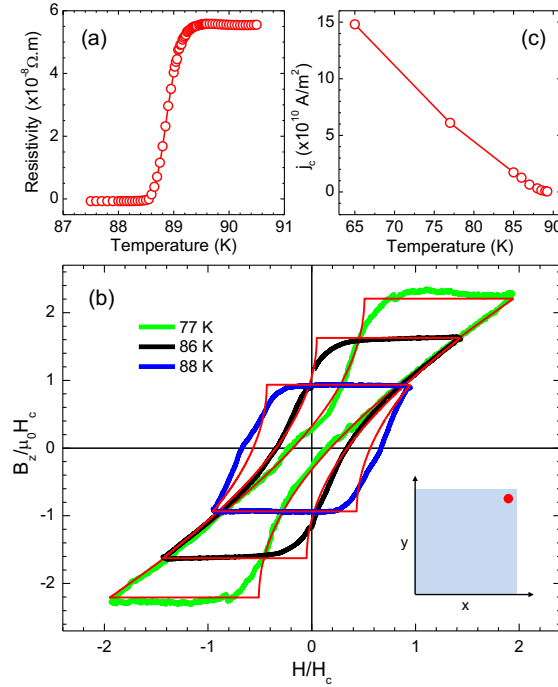
Figure 1. (a) Resistive superconducting transition for the 2G-HTS tape sample after being etched and polished. (b) Scaled magnetic induction hysteresis loops at different temperatures as well as fits to the theoretical model (red lines). (77 K (H_c = 24.4 mT), 86 K (H_c = 5.0 mT), 88 K (H_c = 1.2 mT).) Inset: Map of the SHM field of view showing the position chosen for the local magnetometry measurements (red dot). (c) Temperature-dependence of the superconducting critical current density estimated from fits of the 'local' magnetometry measurements to a theoretical model.

for B_z derived in [11] when the field is decreased from H_{max}

$$B_z^\downarrow(y, H_a, J_c) = B_z(y, H_{max}, j_c) - B_z(y, H_{max} - H_a, 2j_c). \qquad (2)$$

Figure 2(c) shows the penetrated magnetic field profile across the 10 mm wide tape based on equations 1 and 2 when the applied field is reduced from a maximum of $2H_c$ ($H_c = j_c d/\pi$).

Rather than using the position y across the width of the tape as the dependent variable, the model can be used to describe the magnetic field penetration profile at a specific point on the tape as a function of applied field. This is shown in Figure 2(d) at a point 1 mm from the long tape edge for different critical current densities in a maximum applied field intensity of $\pm 2H_{c0}$. Starting from the virgin state, the magnetic flux front first penetrates at exactly the same reduced field value for all traces, and the black curve that corresponds to $j_c/j_{c0} = 2$ lies on top of, and fully overlays, all the other curves in this region. In addition, the lateral gradient of the penetrated

magnetic field across the width of the tape is described by

$$\frac{dB_z}{dy} = \begin{cases} 0 & |y| < b \\ B_c \dfrac{a^2 c}{(a^2 - y^2)\sqrt{y^2 - b^2}} & b < |y| < a \end{cases} \tag{3}$$

This is illustrated in Figure 2(e), and shows that the position of the flux front can be clearly identified by the point where the gradient is singular (at $y = b$). Notice that here again, the black curve that corresponds to $j_c/j_{c0} = 2$ lies on top of, and fully overlays, the other curves from the virgin state up to the first magnetic flux front penetration. This overlay can be noticed by an apparently wider initial segment of the black curve. This highlights an important difference to the Bean critical state in bulk superconductors where the gradient of magnetic induction is predicted to be constant and proportional to j_c. In reality the unphysical singular behaviour predicted by the model would be truncated by the Ginzburg-Landau depairing current density. However, since this is estimated to be almost three orders of magnitude larger than the measured critical current density at our measurement temperatures [13], this would have no appreciable influence on Figure 2(e).

Figure 3 shows a selection of SHM images illustrating the process of flux penetration as the applied magnetic field is increased at 83 K and 77 K. From left to right, one can see the first penetration of the flux front from the tape's virgin state after zero field cooling. The boundary between the mixed state and the central flux-free region determines the flux front whose structure has been shown to be insensitive to edge topology [14]. Although our SHM is capable of deep sub-micron spatial resolution [10, 15], the $1\,\mu$m retraction of the sensor required here limited the overall spatial resolution to the point where single flux line imaging is no longer possible and only bundles of flux lines could be visualised. The penetrating magnetic flux front exhibited very distinctive profiles at different temperatures. At 83 K the flux front penetrated relatively uniformly throughout the whole scan area, as shown in Figure 3(a)-(e). In stark contrast much more localized penetration can be seen in Figure 3(f)-(j) at the lower temperature of 77 K when the flux front penetrates predominantly on the right hand side of the SHM field of view. The magnetic field penetration depth (λ) defines the range of interaction between flux lines and, together with the pinning force, plays an important role in determining the size of the flux line bundles [16]. The penetration depth is temperature-dependent and decreases at lower temperatures [17, 18], reducing the screening current overlap between flux lines and, in conjunction with the increasing vortex pinning force, makes flux bundles more localized. This is reflected in the roughening of the magnetic flux front in the tape whose magnetic field dependence has been attributed to the nonlinear diffusion arising from thermally-activated vortex hopping [14].

A critical current density (j_c) map has been calculated from the sequence of SHM images, as shown in Figure 4 at 83 K, whereby the magnetic induction at every pixel in the image has been analysed as a function of applied field using the critical state model of equations 1 and 2. Here the known position of the Hall sensor within the scan area has been used to adjust the value of y in the theoretical fit. Due to the relatively large time that elapses between sequential SHM images considerable magnetic relaxation occurs due to thermally activated vortex motion (flux creep). This results in a significant reduction of the overall magnetization [19], and estimates of j_c that are somewhat smaller than those of Figure 1(c) which result from the analysis
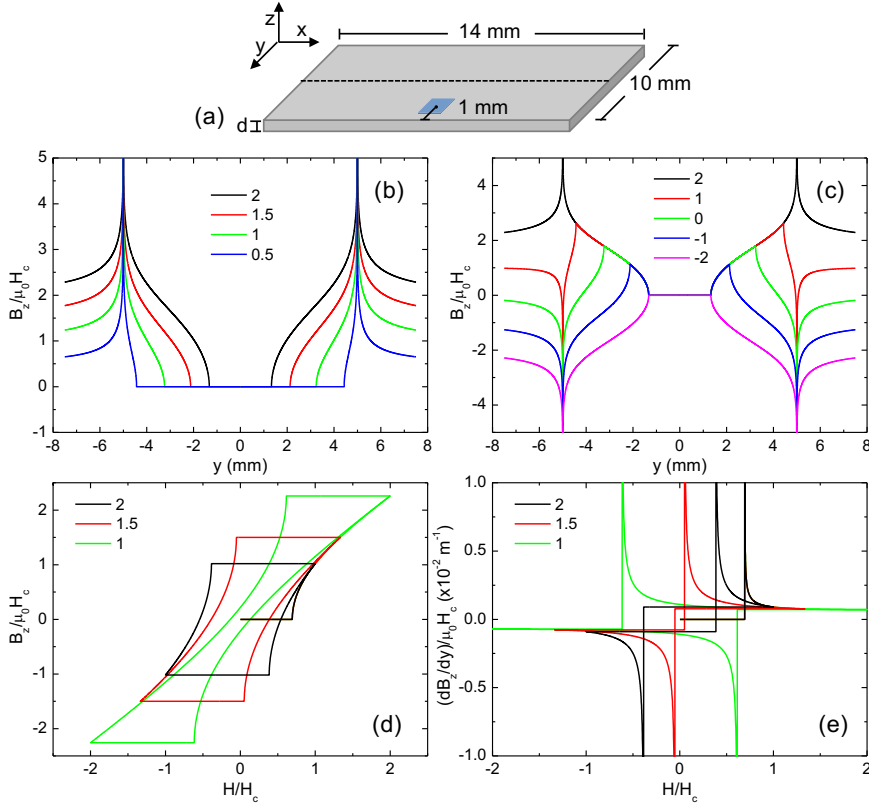
Figure 2. (a) Schematic diagram of the 2G-HTS tape sample with the SHM scan area represented by a blue square (not to scale). (b) Theoretical profiles of the magnetic field penetration across a 10 mm wide thin superconducting strip in perpendicular magnetic fields of $H/H_c = 0.5$, 1, 1.5 and 2 starting from the $H/H_c = 0$ virgin state. (c) Theoretical profiles of the magnetic flux penetration across the strip when the applied perpendicular magnetic field is decreased from $H/H_c = 2$ down to 1, 0, -1 and -2. (d) Scaled magnetic induction hysteresis loops at a point 1 mm from the edge of the tape for a maximum applied magnetic field excursion of $\pm 2H_{c0}$ for critical current densities of $j_c/j_{c0} = 1$, 1.5 and 2. (e) Scaled magnetic induction gradient at a point 1 mm from the edge of the tape for a maximum magnetic field excursion of $\pm 2H_{c0}$ for critical current densities of $j_c/j_{c0} = 1$, 1.5 and 2.

of much faster local magnetometry measurements. The local value of j_c estimated this way shows a substantial variation of about $\pm 7\%$ across the entire field of view.

We observe substantial broadening of the penetrating magnetic flux front at low temperatures. Figure 5(a) and (b) show line scans along the y-axis of the SHM images (across the width of the tape) for increasing applied magnetic fields, starting from the zero field cooled virgin state at 83 K and 77 K respectively. The initial penetration of the flux front can clearly be seen in both figures when the magnetic induction rises abruptly from $B_z \sim 0$. The data show that flux appears to penetrate over a narrower reduced field range at 83 K as compared to much more broadened rise at 77 K. At the same time the normalized gradient dB_z/dy just after initial penetration is clearly quite a bit steeper at the lower temperature. This point is reinforced in Figure 5(c)
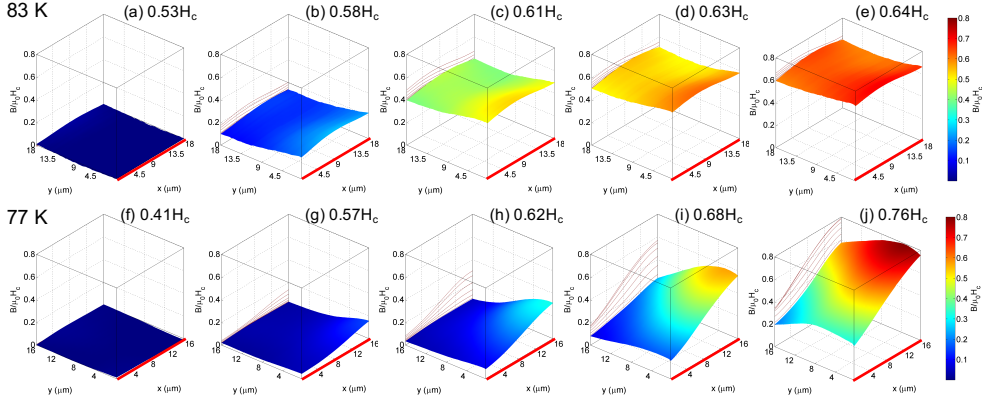
Figure 3. 3D representations of selected SHM images of the magnetic flux front penetration from the long edge of the 2G-HTS tape (indicated by the red line) at (a)-(e) 83 K (H_c = 7.2 mT) and (f)-(j) 77 K (H_c = 24.4 mT) as the applied magnetic field is gradually increased.
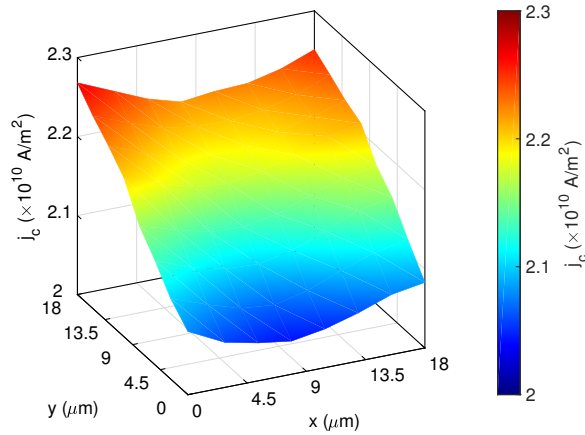
Figure 4. Calculated critical current density (j_c) obtained from fitting the magnetic induction at each pixel of the SHM image as a function of applied field to a theoretical model at 83 K, for a maximum applied magnetic field of ±4.8 mT.

and (d) where the gradient along half of the y-axis (9-18 μm and 8-16 μm respectively) has been plotted as a function of applied magnetic field for each temperature. Here the square symbols and magenta line correspond to the first flux front penetration starting from the zero field cooled virgin state. The reversed flux front penetration is shown by the circle symbols and a blue line. The triangle symbols and dark green line show the effect of reversing the applied field once again. At 83 K the data are close to the expected theoretical behaviour calculated from equation 3 but the singularity at initial penetration has been very substantially smeared out. In contrast the behaviour at 77 K is very different to that expected from the model. The singular penetration peak is broadened out over a wide range of applied fields and the measured values of dB_z/dy are in general much larger than predicted.
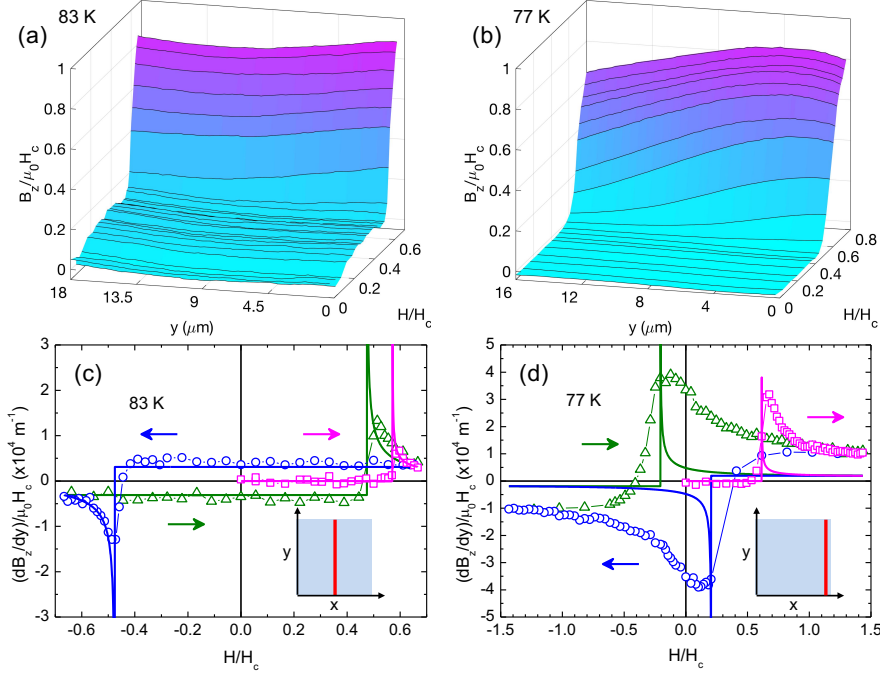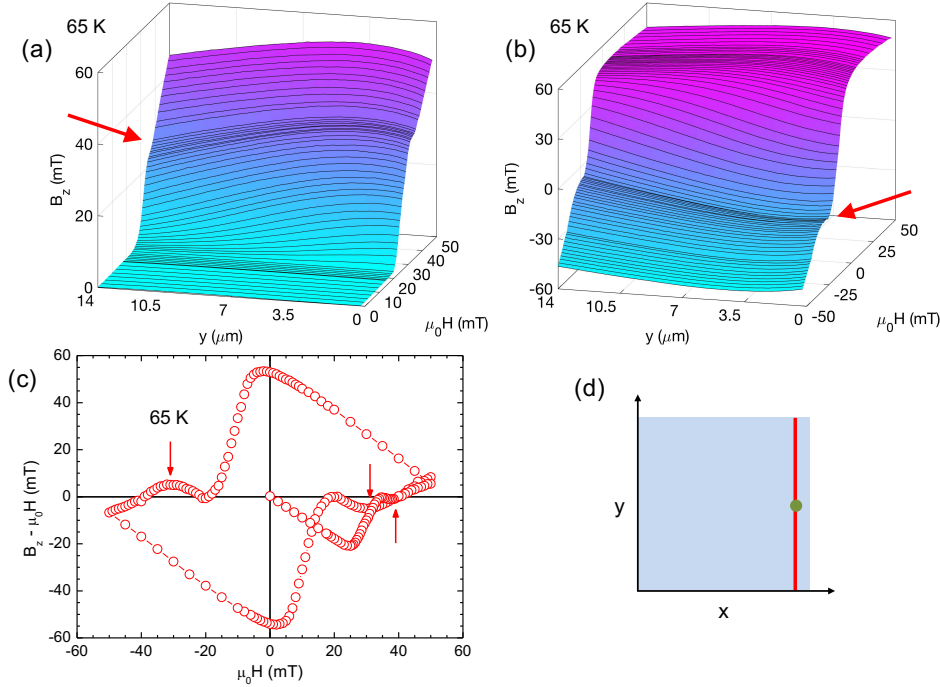
Figure 5. Line scans along the y-axis of SHM images as a function of applied magnetic field spanning initial magnetic flux penetration at (a) 83 K (H_c = 7.2 mT) and (b) 77 K (H_c = 24.4 mT). Normalized gradient of the penetrating magnetic flux front, dB_z/dy, along the y-axis of SHM images as a function of applied magnetic field at (c) 83 K and (d) 77 K. The symbols show the experimental data while the solid lines show the theoretical values obtained from equation 3. Insets: Schematic diagrams of the SHM scan area indicating the lines where the magnetic induction in (a) and (b) and gradients in (c) and (d) have been measured corresponding to the centres of penetrating flux bundles (red lines).

Figure 5 indicates a pronounced onset of local vortex-bundle formation at 77 K. Since the currents circulating around bundles lead to higher local magnetic fields than along straight flux fronts, we associate this with the higher local dB_z/dy and faster flux front penetration observed. While some inhomogeneity of the penetrating flux front is also visible at 83 K, this is not nearly as pronounced as at 77 K. This pronounced increase in the flux front inhomogeneity at the lower temperature could be linked to a fairly abrupt reduction in the size of bundles formed due to collective pinning at many pinning centres. For thin films, the correlated bundle radius is given by, $R_b = C_{66}a/f\sqrt{n}$, where C_{66} is the shear elastic modulus, a the mean vortex spacing, f the pinning force and n the areal density of pinning sites [20]. Noting that $C_{66} \sim \bar{B}/\lambda^2$ [21], where $\bar{B}$ is the average flux density, and assuming that more pinning sites are coming into play at lower temperatures as the characteristic superconducting lengthscales reduce, then the pinning force and the density of pinning sites term, $f\sqrt{n}$, can increase faster than $1/\lambda^2$. Thus, we can expect a decreasing bundle size as the temperature is decreased as observed. Furthermore, the processes of reverse

flux front penetration and annihilation exhibit different dynamics to the first flux front penetration, suggesting that the vortex bundle structure is influenced by the surrounding environment. This can be seen when comparing the magenta line/squares with the blue line/circles in Figure 5(c) and (d), highlighting the complex flux line dynamics in these tapes.

Figure 6. Line scans along the y-axis of SHM images at 65 K ($H_c = 59.2$ mT) for different applied magnetic fields (a) for the first flux front penetration and (b) for the subsequent reverse flux front penetration. (c) 'Local' magnetization loop as a function of applied field measured at a single pixel of the SHM images as a function of applied magnetic field at 65 K. Vertical red arrows indicate fishtail-like peaks in the local magnetization. (d) Schematic representation of the SHM scan area indicating the line where the magnetic induction has been measured in (a) and (b) (red line) and the pixel where the data in (c) (green dot) have been constructed.

'Local' magnetization and SHM measurements have also been extended down to the sub-cooled liquid nitrogen temperature of 65 K, at which 2G-HTS tape performance is known to improve strongly including a substantial increase in critical current [22]. Line scans along the y-axis of SHM images as the applied magnetic field is increased from the zero field-cooled state are shown in Figure 6(a) and reveal a pronounced flattening at μ_0H $\sim$ 40 mT indicated by the red arrow. Likewise, when the direction of magnetic field sweep is reversed a similar flat region can be seen at μ_0H $\sim$ -30 mT as shown in Figure 6(b). Interestingly, peaks are observed in the M_l-H loops which resemble the so-called fishtail effect, as indicated by vertical red arrows in Figure 6(c). Here we present two possible explanations for the observed phenomena. The peaks shown in Figure 6(c) appear to occur due to a field-dependent

increase in the critical current near the edge of the tape that screens out additional flux penetration over a narrow range of fields. We speculate that this arises due to a "matching effect" when the density of flux lines near the edge of the tape approximately equals the density of strong pinning centres in the YBCO thin film. As a consequence, the superconducting critical current increases at the edge of the tape, increasing the average value of dB_z/dy there and preventing additional flux from penetrating to the SHM scan area. Hence the flux detected by the scanning Hall probe remains locked over a narrow band of applied fields of approximately $\mu_0 \Delta H$ ~ 10 mT. Using the measured matching field of $B_z \sim 40$ mT as a lower bound on the relevant magnetic induction, the density of strong pinning sites can be estimated as $B \sim \phi_0/a^2$ where ϕ_0 is the magnetic flux quantum and a is the mean spacing between pinning centres. This allows us to estimate an upper bound of $a \sim 230$ nm which we can compare with the mean spacing between Dy_2O_3 second phase particles introduced to enhance vortex pinning. An earlier STEM tomography study [23] of a Dy-doped superconducting YBCO thin film from a very similar tape revealed second phase particles with diameter in the range of 10-100 nm and average density of 1538 particles/μm^2 (71 particles/0.06 μm^3, 1.3 μm thick YBCO film). Vortex 'core' pinning centres should ideally have a radius comparable to the coherence length and one might expect that only the smallest of these particles will be effective. Our estimated matching field suggests that indeed only a small fraction of the particles act as strong pinning sites corresponding to a density of ~ 20 particles/μm^2. However, we note that the magnetic induction at the edge of the strip will be greatly enhanced due to the sample geometry and associated demagnetization effects [11], and the actual matching pinning site density may be very much higher than our lower bound estimate. These peaks were probably not observed in measurements at temperatures at 77 K and above because the applied field was limited to $\mu_0 H < 35$ mT, and the matching condition would not have been reached.

An alternative explanation for the observed peaks relates to the possible existence of a field-driven disordering transition. In an increasing magnetic field the system could undergo a transition from a relatively well ordered Bragg glass phase [24, 25], to a disordered glassy phase [26, 27], as determined by the fine balance between elastic, pinning and thermal energies [28]. Therefore, in this scenario the peak is a dynamic response resulting from additional pinning due to a more effective interaction with the vortex pinning landscape in the disordered glassy phase. Given the very high levels of disorder present in these 2G-HTS films the presence of a well-ordered Bragg glass phase seems improbable under any conditions, and an explanation in terms of matching effects seems much more likely.

4. Conclusions

The critical state of a second generation superconducting high temperature tape has been studied and mapped. The Brandt and Indenbom critical state model describes the vortex system relatively well at temperatures close to T_c, when thermal energy plays a larger role in comparison to typical pinning energies. However, at lower temperatures our experimental results deviate markedly from the critical state model with strong suppression of the singular slope, dB_z/dy, predicted at the flux front. Our measurements exhibit dramatically different flux front roughening and profile broadening behaviours at different temperatures. Penetrating flux fronts exhibit much more localized bundle-like behaviour at low temperatures, reflecting the temperature-

dependence of the pinning force and the active pinning site density which determine the typical size of flux bundles. Fishtail-like magnetization peaks have also been observed in local magnetization measurements at 65 K which we link to an increase in the critical current density near the edge of the films, probably arising due to a magnetic field matching effect. These findings contribute importantly to a more detailed understanding of flux line phenomena in 2G-HTS tapes.

Acknowledgments

References

[1] Maguire J F, Schmidt F, Bratt S, Welsh T E and Yuan J 2009 *IEEE Trans. Appl. Supercond.* **19** 1692–1697 URL https://doi.org/10.1109/TASC.2009.2018221

[2] Schmidt W, Gamble B, Kraemer H P, Madura D, Otto A and Romanosky W 2010 *Supercond. Sci. Technol.* **23** 014024 URL http://stacks.iop.org/0953-2048/23/i=1/a=014024

[3] Haran K S, Kalsi S, Arndt T, Karmaker H, Badcock R, Buckley B, Haugan T, Izumi M, Loder D, Bray J W, Masson P and Stautner E W 2017 *Supercond. Sci. Technol.* **30** 123002 URL http://stacks.iop.org/0953-2048/30/i=12/a=123002

[4] Leroux M, Kihlstrom K J, Holleis S, Rupich M W, Sathyamurthy S, Fleshler S, Sheng H P, Miller D J, Eley S, Civale L, Kayani A, Niraula P M, Welp U and Kwok W K 2015 *Appl. Phys. Lett.* **107** 192601 URL https://doi.org/10.1063/1.4935335

[5] Yamasaki H and Yamada H 2017 *Physica C* **542** 46 – 54 URL https://doi.org/10.1016/j.physc.2017.09.003

[6] Trastoy J, Ulysse C, Bernard R, Malnou M, Bergeal N, Lesueur J, Briatico J and Villegas J E 2015 *Phys. Rev. Appl.* **4**(5) 054003 URL https://link.aps.org/doi/10.1103/PhysRevApplied.4.054003

[7] Kwok W K, Welp U, Glatz A, Koshelev A E, Kihlstrom K J and Crabtree G W 2016 *Rep. Prog. Phys.* **79** 116501 URL http://stacks.iop.org/0034-4885/79/i=11/a=116501

[8] Dinner R B, Moler K A, Beasley M R and Feldmann D M 2007 *Appl. Phys. Lett.* **90** 212501 URL https://doi.org/10.1063/1.2740610

[9] Dinner R B, Moler K A, Feldmann D M and Beasley M R 2007 *Phys. Rev. B* **75**(14) 144503 URL https://link.aps.org/doi/10.1103/PhysRevB.75.144503

[10] Oral A, Bending S J and Henini M 1996 *Appl. Phys. Lett.* **69** 1324–1326 URL https://doi.org/10.1063/1.117582

[11] Brandt E H and Indenbom M 1993 *Phys. Rev. B* **48**(17) 12893–12906 URL https://link.aps.org/doi/10.1103/PhysRevB.48.12893

[12] Rupich M W, Li X, Thieme C, Sathyamurthy S, Fleshler S, Tucker D, Thompson E, Schreiber J, Lynch J, Buczek D *et al.* 2009 *Supercond. Sci. Technol.* **23** 014015 URL http://stacks.iop.org/0953-2048/23/i=1/a=014015

[13] Lang W, Puica I, Peruzzi M, Lemmermann K, Pedarnig J D and Bäuerle D 2005 *Phys. Stat. Sol. (c)* **2** 1615–1624 URL https://onlinelibrary.wiley.com/doi/abs/10.1002/pssc.200460801

[14] Surdeanu R, Wijngaarden R J, Visser E, Huijbregtse J M, Rector J H, Dam B and Griessen R 1999 *Phys. Rev. Lett.* **83**(10) 2054–2057 URL https://link.aps.org/doi/10.1103/PhysRevLett.83.2054

[15] Marchiori E, Curran P J, Kim J, Satchell N, Burnell G and Bending S J 2017 *Sci. Rep.* **7**(45182) URL https://www.nature.com/articles/srep45182

[16] Blatter G, Feigel'man M V, Geshkenbein V B, Larkin A I and Vinokur V M 1994 *Rev. Mod. Phys.* **66**(4) 1125–1388 URL https://link.aps.org/doi/10.1103/RevModPhys.66.1125

[17] Fiory A T, Hebard A F, Mankiewich P M and Howard R E 1988 *Phys. Rev. Lett.* **61**(12) 1419–1422 URL https://link.aps.org/doi/10.1103/PhysRevLett.61.1419

[18] Annett J, Goldenfeld N and Renn S R 1991 *Phys. Rev. B* **43**(4) 2778–2782 URL https://link.aps.org/doi/10.1103/PhysRevB.43.2778

[19] Yeshurun Y, Malozemoff A P and Shaulov A 1996 *Rev. Mod. Phys.* **68**(3) 911–949 URL https://link.aps.org/doi/10.1103/RevModPhys.68.911

[20] Larkin A I and Ovchinnikov Y N 1979 *J. Low Temp. Phys.* **34** 409–428 URL https://doi.org/10.1007/BF00117160

[21] Brandt E H 2002 *Braz. J. Phys.* **32** 675–684 URL https://doi.org/10.1590/s0103-97332002000400002

[22] Llambes J C, Hazelton D, Duval J, Albertini M, Repnoy S, Selvamanickam V, Majkic G, Kesign I, Langston J, Steurer M, Bogdan F, Hauer J, Crook D, Ranner S, Williams T and Coleman M 2011 *IEEE Trans. Appl. Supercond.* **21** 1206–1208 URL https://doi.org/10.1109/tasc.2010.2101572

[23] Ortalan V, Herrera M, Rupich M and Browning N 2009 *Physica C* **469** 2052–2059 URL https://doi.org/10.1016/j.physc.2009.08.012

[24] Giamarchi T and Le Doussal P 1995 *Phys. Rev. B* **52**(2) 1242–1270 URL https://link.aps.org/doi/10.1103/PhysRevB.52.1242

[25] Shibata K, Nishizaki T, Sasaki T and Kobayashi N 2002 *Phys. Rev. B* **66**(21) 214518 URL https://link.aps.org/doi/10.1103/PhysRevB.66.214518

[26] Fisher D S, Fisher M P A and Huse D A 1991 *Phys. Rev. B* **43**(1) 130–159 URL https://link.aps.org/doi/10.1103/PhysRevB.43.130

[27] Koch R H, Foglietti V, Gallagher W J, Koren G, Gupta A and Fisher M P A 1989 *Phys. Rev. Lett.* **63**(14) 1511–1514 URL https://link.aps.org/doi/10.1103/PhysRevLett.63.1511

[28] Nishizaki T and Kobayashi N 2000 *Supercond. Sci. Technol.* **13** 1–11 URL https://doi.org/10.1088/0953-2048/13/5/501